Mathematical Biosciences and Engineering

MBE, 20(5): 8727–8744.
DOI: 10.3934/mbe.2023383
Received: 16 November 2022
Revised: 12 January 2023
Accepted: 19 January 2023
Published: 07 March 2023

http://www.aimspress.com/journal/MBE

Research article

Brain image fusion-based tumour detection using grey level co-occurrence matrix Tamura feature extraction with backpropagation network classification

R. Bhavani[1,*] and K. Vasanth[2]

[1] Department of ECE, Sathyabama Institute of Science and Technology, Chennai 600119, India
[2] Department of ECE, Vidya Jyothi Institute of Technology, Hyderabad 500075, India

* **Correspondence:** Email: bhavanidinesh149@gmail.com.

Abstract: Most challenging task in medical image analysis is the detection of brain tumours, which can be accomplished by methodologies such as MRI, CT and PET. MRI and CT images are chosen and fused after preprocessing and SWT-based decomposition stage to increase efficiency. The fused image is obtained through ISWT. Further, its features are extracted through the GLCM-Tamura method and fed to the BPN classifier. Will employ supervised learning with a non-knowledge-based classifier for picture classification. The classifier utilized Trained databases of the tumour as benign or malignant from which the tumour region is segmented via k-means clustering. After the software needs to be implemented, the health status of the patients is notified through GSM. Our method integrates image fusion, feature extraction, and classification to distinguish and further segment the tumour-affected area and to acknowledge the affected person. The experimental analysis has been carried out regarding accuracy, precision, recall, F-1 score, RMSE and MAP.

Keywords: medical image analysis; image fusion; feature extraction; classification; tumor

1. Introduction

A tumour develops when aberrant cells divide uncontrollably, generating a mass that can obstruct the tissue's or organ's normal function. Tumours are classified based on their origin as well as cell

types. Early stages of tumours present mostly in the cerebrum, whereas secondary tumours spread to the brain from other body areas [1]. Tumours can be carcinogenic or benign. A malignant brain tumour grows much faster than a benign brain tumour and is more likely to infect nearby tissues. As a result, a primary malignant brain tumour has a dismal prognosis and significantly lowers cognitive function and quality of life [2]. Brain and nervous system cancers are the tenth largest cause of death and the third most common malignancy among teenagers and adults. Male and female patients with malignant brains have a five-year survival rate of 34% and 36%. Gliomas, the most common cerebral tumour in adults, account for about 80% of malignant cases. According to research, patients with low-grade gliomas (LGG) have a ten-year survival rate of roughly 57%.

Environmental factors such as excessive use of artificial chemicals or genetic factors can both contribute to the development of a brain tumour. Radiotherapy, chemotherapy, and surgery are all choices for treatment. The earlier a brain tumour is found, the better the prognosis and the more therapeutic choices available. MRI, BIOPSY and SPECT (single photon emission computed tomography) scans are technologies used to diagnose a brain tumour. Magnetic resonance imaging (MRI) is the most common method, a non-invasive imaging tool that gives distinct tissue contrast. However, there are restrictions due to the unpredictable, random, and uneven size, shape, and location of brain tumours. Furthermore, given the amount of data to be processed, non-autonomous tumour partitioning takes a long time and is a labour-intensive, difficult, and mostly subjective task, lowering accuracy [3].

Image fusion enhances data content by integrating two or more photos using a specific method. This research effort might benefit from a case study on the impact of image fusion algorithms on classification accuracy for remote sensing applications. For the analysis, they used a Landsat 7 ETM+ image. AIF, MMT, PCA, HSV and the proven fusion technique were all investigated. Maximum likelihood classifier, object-based classification, and SVM classifier [4] all used fusion findings. BT was devised to visually increase the contrast between the low and high ends of the image histogram. If original scene radiometry must be retained, BT produces spectral deterioration, which should not be used. When applying pixel-based classifiers, the bravery transform produced a final image with a low dynamic range and substantial misclassification. The discrete classes from the training dataset were not assigned via HSV fusion. Because it can distinguish a picture's high- and low-frequency components, another technique called PCA performed better. The MMT fusion method resulted in "Speckle" noise in classification and poor edge recognition. To depict abrupt peaks and discontinuities, wavelet transforms are used. Shift sensitivity and directional selectivity are two shortcomings of the wavelet transform [5].

Using computer algorithms to execute picture processing on digital images is known as digital image processing. It approves many methods to be applied to input methods and avoids noise and background distortion throughout the process. Medical image processing is an automatic system used to detect the problems of the inner organs in the human body. Medical imaging produces seen pix of inside structures of the physique for scientific and medicinal learning about and remedies as properly as a considered view of the feature of indoor tissues. It contains many methods and steps to detect and give the result without any time consumption, which involves pre-processing and enhancement of image, segmentation, feature extraction, and classification using SVM [6].

The contribution of this research is as follows:

1) To increase efficiency, MRI and CT images are chosen and fused after undergoing preprocessing and SWT-based decomposition stage;

2) To extract the features of a fused image using the GLCM-Tamura method, which is fed to the BPN classifier;

3) The experimental analysis has been carried out regarding accuracy, precision, recall, F-1 score, RMSE, and MAP.

2. Related works

The guided image filter is proposed for integrating MRI and CT images in the literature [7]. The quiet data from images were recovered (GF), and the guided filter provided the best edge-preserving information. [8] proposed image fusion using a guided filter, in which GF functions as a boundary smoothing as well as preserving operator comparable to a well-known bilateral filter. It has improved borders' performance. It is thought to be related to the Laplacian matrix. It is a non-estimated linear time approach with a density that is independent of mask size. [9] also introduced the multi-resolution singular value decomposition (MSVD) fusion technique. WT and MSVD looked similar. Signals are split into low-pass and high-pass finite impulse filters in this method. The filter output was reduced and decomposed into the next level at each decomposition level, and this process was repeated to achieve the next succeeding levels. Furthermore, [10] compares MSVD, WT, and Laplacian pyramid approaches. According to experimental results, MSVD outperforms WT regarding RMSE, which is low, and PSNR, which is high. [11] also introduced a pixel-level IF approach based on PCA and WT. PCA is a statistical approach for converting a series of observations of a possibly correlated variable into the main and a dimension reduction technique based on orthogonal transformation. PCA's primary disadvantage is spectrum degradation and colour distortion. A survey of several multi-spectral image fusion algorithms was published in [12]. In contrast, the author of [13] compared various medical IF approaches. Work [14] presented a novel medical image fusion paradigm for improving spatial resolution by merging high-resolution anatomic images with functional images. Algorithms used to segment brain tumours can be classified as classic or non-autonomous procedures and deep-learning techniques. Regularized non-negative matrix factorization (NMF) and CAD methods that use computing techniques like K-means clustering, PCA and SVM are examples of the former [15]. Work [16] used fuzzy clustering with region-growing to achieve a 73% segmentation accuracy using instances scanned by T1 and T2-weighted sequences. The author of [17] tested various clustering methods for brain tumour segmentation and found that k-means, fuzzy k-mean. Work in [18] rated brain tumours using SVM as a foundation, incorporating 38 first-order or second-order statistical measures. DL methods have recently gained popularity among researchers because they automate the extraction of a complicated set of features from data. Tumour segmentation was accomplished using the LinkNet network in the study [19]. Initially, a single LinkNet network segmented all seven training datasets. Later, a CNN method was created for the autonomous extraction of the most common tumour types without the need for preprocessing. A single network received a die score of 0.73, whereas many systems received a score of 0.79. By feeding the 3D MRI image voxels into a two-dimensional CNN method, the study [20] uses several CNN for brain tumour segmentation. The result is a segmentation of brain tumours rather than a categorization. Work [21] combines SVMs with artificial neural networks to grade brain cancers (ANNs). The learning process inaccuracy was minimized by ANNs, resulting in a 97.44% accuracy. However, because the number of photos used in the training process in this method is very low, acceptability questions for datasets with a large number of images arise. The author in [22] studied the ImageNet dataset. They developed a high-performance object detector

based on CNN ideas that demonstrated a 70% improvement in accuracy over previous studies on the ImageNet dataset. Several academics have worked in the domain of picture fusion of multimodal images using various methodologies in recent years, but some challenges, such as edge visibility and blurring edges, still need to be solved. As a result, a new multimodal image fusion method must be created to overcome the existing state-of-the-art systems' shortcomings.

3. Materials and methods

This section discusses the novel technique for increasing the efficiency of image fusion using GLCM-Tamura method-based feature extraction with a BPN classifier. The proposed architecture is represented in Figure 1. For analysis, images such as MRI and CT scans are acquired from http://kaggle.com. Before performing the image fusion method, the input images were registered. The discrete cosine transform was utilized to produce picture fusion, and fused images were obtained. Thirty characteristics were retrieved from fused images and sent into three classifiers as input. A classifier's accuracy, precision, recall, specificity, and F1 score are used to evaluate its performance. When characteristics derived from individual input photos were provided to classifiers, these results were compared to classifier findings. High-performance indicators imply that classifiers are performing well.

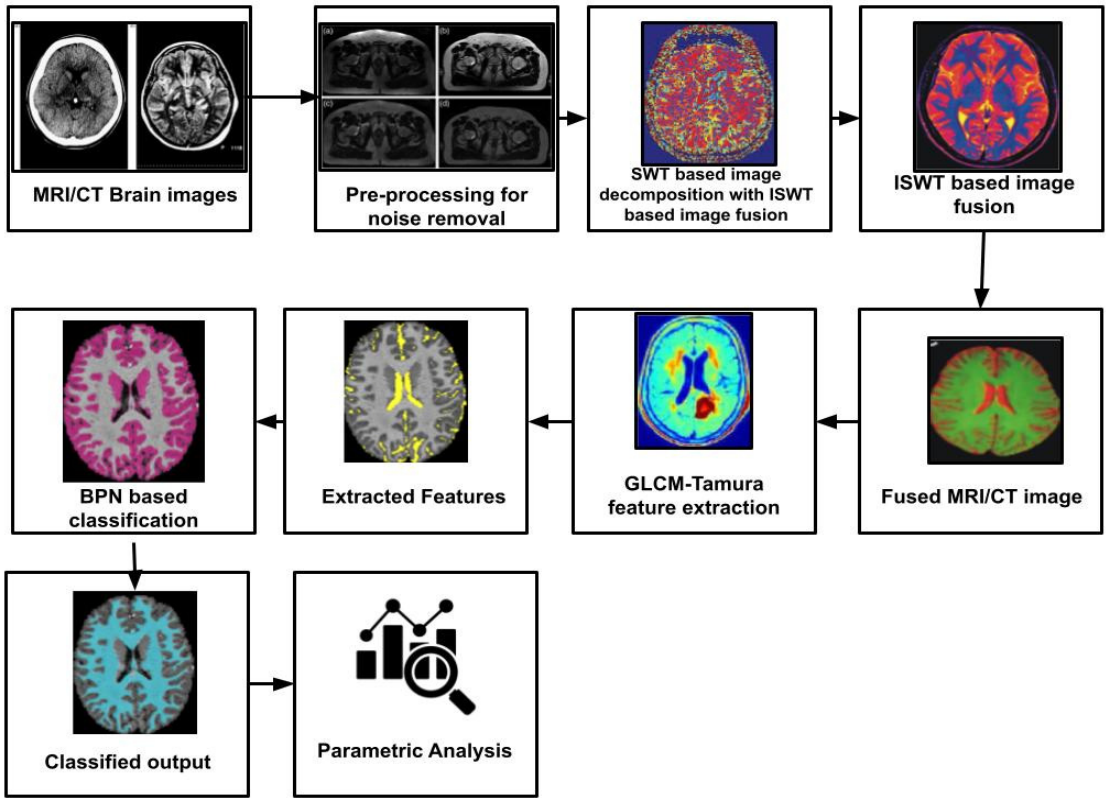

Figure 1. Overall proposed architecture.

In medical imaging, enhancement refers to the employment of algorithms to improve image clarity and ensure the best possible display of all digital computer processing. It proves to be beneficial

as well as crucial in medical diagnosis. This may aid human or computer interpretation. The goal of enhancement is to improve the quality of an image. It reduces noise, increases contrast, emphasizes edges, and changes shapes. Researchers are interested in multiscale approaches for picture contrast enhancement, particularly wavelet transform. This technique enhances the edges of the segmented region of interest. The second algorithm improves the segmentation process by adjusting the contrast of the source image. The second morphological contrast enhancement approach is discussed here. [10] provides a thorough theory of mathematical morphology. We discovered that arranging the element as a disc with a radius of 30 produces the optimum morphological algorithm performance. We convolve obtained image using a 3 × 3 Gaussian low-pass filter specified in Eq (1) [10] to increase the contrast enhancement:

$$LPGF = (0.0071\ 0.0835\ 0.0071\ 0.0835\ 0.9859\ 0.0835\ 0.0071\ 0.0835\ 0.0071)$$

3.1. SWT-based decomposition stage

A wavelet is a transitory signal that contains finite-energy frequencies. A wavelet transform is a technique for filtering signal characteristics across frequencies and time. The DWT is a wavelet transform that has been sampled. The DWT is applied to an image's rows first, then to its columns. At each level of the transform, the filters are updated by adding zeros between their coefficients, a process known as decimation. The discrete wavelets operate as high and low-pass frequency filters thanks to a decimated algorithm. Figure 2 shows the DWT processing.

The 2D SWT, unlike the DWT, is based on the idea of no decimation, which means it is undecimated [15]. SWT process is depicted in Figure 3. The SWT uses the DWT but eliminates both down and up-sampling in forward and inverse transforms. It uses the SWT at each level of the image, maintaining precise coefficients and utilizing low-frequency information. Image fusion with SWT can be achieved by registering two source images and then applying the SWT to both input images.

After that, a fusion decision map is created. The map is created using pre-set fusion rules. The Inverse Stationary WT is applied to the merged image to recreate it (ISWT).

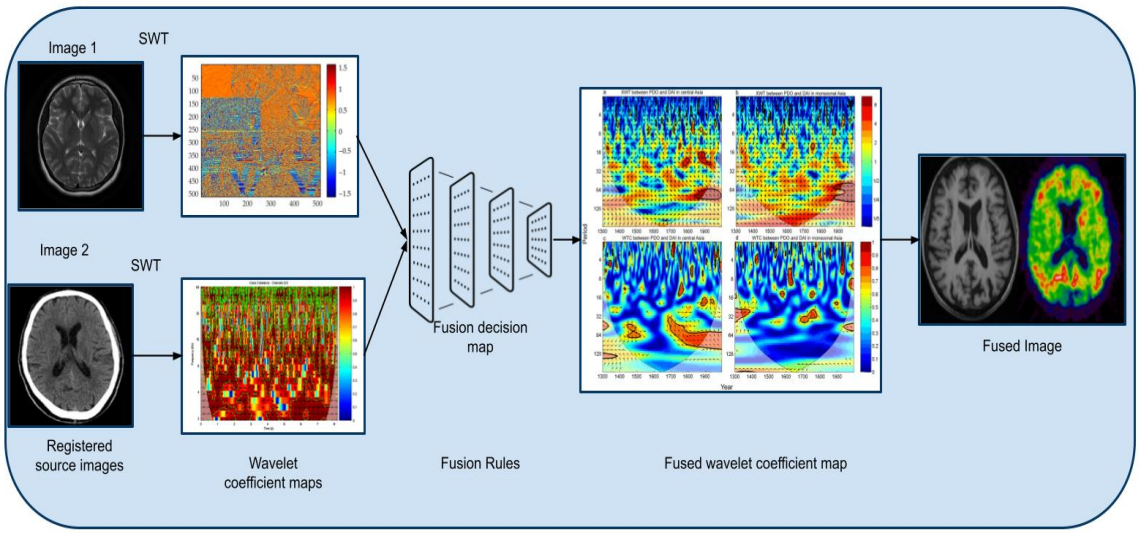

Figure 2. Discrete wavelet transform.

Fusion algorithm: The algorithm for image fusion is defined as follows:

1) Decompose two source images into three detail subbands and one approximation subband using SWT at one level (HL, LH, HH and LL bands).

2) Then take an average of the photos' approximate sections.

3) Take absolute values of the image's horizontal details and subtract the second component from the first.

4) $D = (abs\ (H1L2) - abs\ (H2L2)) >= 0$

5) For the fused horizontal section, multiply D and the horizontal detail of the first image element by element.

6) Determine D for the vertical as well as diagonal regions of the image as well as get fused vertical as well as details.

7) Fusion at the first level follows the same procedure.

8) The inverse stationary WT is employed to create a fused image.

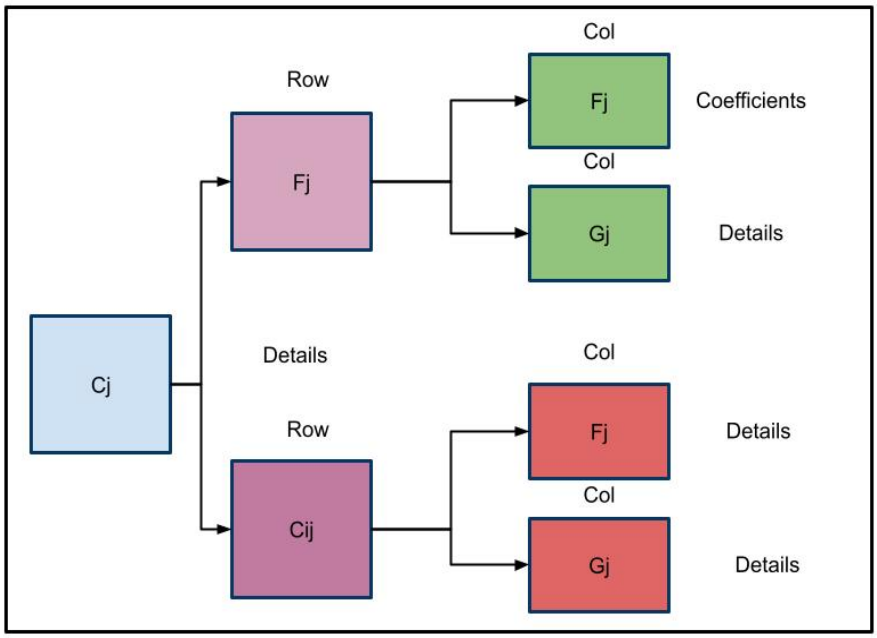

Figure 3. Stationary wavelet transform.

3.2. GLCM-Tamura method-based feature extraction

GLCM is used to extract second-order statistics. The GLCM method determines how certain grey levels interact with one another. The matrix calculates the relative frequency of grey-level combinations co-occurring inside pairs of pixels in a specified spatial connection. Evaluate how often a grey level l I occurs in place provided by relationship operator, q. $M(i,j)$ is a measure of joint probability in which a pair of points must meet q with values l I l (j) (j). An angle θ and a distance d represent a relationship operator. The co-occurrence matrix has dimension Nm, and the mean of x and y is described in Eq (1):

$$\mu_x = \sum_{t=1}^{N_{m_1}} \quad i_x(i), \mu_y = \sum_{t=1}^{N_m} \quad m_y(j) \tag{1}$$

Moreover, σ_x and σ_y are standard deviations of m_x and m_y, respectively and defined in Eq (2):

$$\sigma_x = \left(\sum_{i=1}^{N_m} \quad m_x(i)(i-\mu_x)^2\right)^{1/2}, \sigma_y = \left(\sum_{i=1}^{N} \quad m_y(j)\left(j-\mu_y\right)^2\right)^{1/2} \tag{2}$$

From M(i,j), μ_x, μ_y, σ_x and σ_y, 14 texture statistical measures of texture features are extracted such as contrast, correlation, data measure of correlation, inverse difference, correlation data measure, sum variance, difference variance, moment, sum average, entropy, difference, and sum entropy local variations, the joint likelihood of occurrence of specified pixel pairings, the sum of squared pixel elements, and proximity of distribution of elements are all attributes that can be measured. GLCM similarity has been calculated by Eq (3),

$$\sum_{n=0}^{0-1} \quad n^2\left\{\sum_{i=1}^{0} \quad \sum_{j=1}^{0} \quad P(i,j)\right\}, |i-j| = n \tag{3}$$

Correlation:

$$\sum_{i=0}^{a-1} \quad \sum_{i=0}^{\sigma-1} \quad \frac{(i-\mu_i)(j-\mu_j)P(i,j)}{\sigma_i\sigma_j} \tag{4}$$

Energy:

$$\sum_{i=0}^{G-1} \quad \sum_{i=0}^{G-1} \quad \{P(i,j)\}^2 \tag{5}$$

Homogeneity:

$$\sum_{i}^{G-1} \quad \sum_{i}^{G-1} \quad \frac{P(i,j)}{1+|i-j|} \tag{6}$$

Entropy:

$$-\sum_{i=0}^{0-1} \quad \sum_{j=0}^{0-1} \quad P(i,j) \times log(P(i,j)) \tag{7}$$

3.3. Tamura features

Coarseness, contrast, directionality, line-likeness, regularity, and roughness are six texture qualities relevant to the human visual perception that Tamura extracted.

Coarseness: A distance of spatial variations of grey levels measures the texture scale. The procedure to evaluate the coarseness is as follows: At every pixel (x, y), six averages for windows of size $2^n \times 2^n, n = 0,1, \ldots,5$, around pixel are computed. The average is given as Eq (8):

$$A(x,y) = \sum_{i1=x=2^{x-1}}^{x+2^{x-4}} \quad \sum_{j=y^{2+1}}^{y+2^{x-4-1}} \quad \frac{f1(i1,jl)}{2^{2a}} \tag{8}$$

where $fl(11, jl)$ is gray level value at pixel (x, y). Absolute differences $E_n(x, y)$ between pairs of non-overlapping averages in horizontal as well as vertical directions are computed for each pixel which is given as Eqs (9) and (10):

$$E_{t,x}(x,y) = |A_s(x + 2^{n-1}, y) - A_n(x - 2^{n-1}, y)| \quad (9)$$

$$E_{0,v}(x,y) = |A_s(x, y + 2^{n-1}) - A_n(x, y - 2^{n-t})| \quad (10)$$

The optimal size is determined as 2^n given by eqn at every pixel by finding the value of n that increases the difference $E_n(x,y)$in either direction as in Eq (11)

$$Sl_{teet}\,(x,y) = 2^n \quad (11)$$

The Coarseness feature is evaluated by averaging $Sl_{bea}\,(x,y)$ over the entire image as shown in Eq (12):

$$Coarseness\ = \frac{1}{m\times n}\sum_{i=1}^{m}\quad \sum_{j=1}^{n}\quad Sl_{bet}\,(il,jl) \quad (12)$$

Contrast: Contrast measures how grey levels $g; g = 0, 1, \ldots,\ _{GMOs}$ vary in the image and how much their variation is influenced by black or white. Variance, σ^2 and kurtosis, μ_4/σ_4, define the contrast. The value $nl = 0.25$ is suggested as best for discriminating the textures by Eq (13):

$$Contrast\ = \frac{\sigma}{\left(\frac{\mu_4}{\sigma_4}\right)^{al}} \quad (13)$$

Where:

$\sigma =$ The standard deviation

$\mu_4 =$ The fourth moment about mean

$\sigma_4 =$ Variance squared

Directionality: Directionality is invariant to orientation [12]. Firstly, each sub-image was convolved with an edge filter to evaluate horizontal and vertical differences, d_b and d_v. The convolution of image $X(n_1, n_1)$ is done with following 3×3 operators given by Eq (14):

$$-1\ 0\ 1\ 1\ 1\ 1\ -1\ 0\ 1\ 0\ 0\ 0\ -1\ 0\ 1\ -1\ -1\ -1 \quad (14)$$

And then for every position (n_0, n_1) as given in Eq (15):

$$\theta = \frac{\pi}{2} + tan^{-1}\frac{d_v(n_0,n_1)}{d_k(n_0,n_1)} \quad (15)$$

The directionality is evaluated as the sum of second moments around every peak from valley to valley after these values have been histogramming in a sixteen-bin histogram.

3.3.1. Feature extraction using SWT-GLCM and Tamura

In decomposing a discrete wavelet, the output is the original image's coefficients (approximation, horizontal, vertical and diagonal). The approximation carries little energy, so is skipped from the analysis. The GLCM descriptors like contrast, correlation, energy, homogeneity and entropy for four offsets are calculated for horizontal, vertical and diagonal coefficients.

Similarly, Tamura features like coarseness, contrast and directionality are calculated for horizontal, vertical and diagonal coefficients, thus giving a total of 69 features listed as. DWT-GLCM-TAMURA = {contrast 1, correlation 1, energy 1, homogeneity 1, entropy 1, contrast 2, correlation 2, energy 2, homogeneity 2, entropy 2, contrast 3, correlation 3, energy 3, homogeneity 3, entropy 3,

contrast 4, correlation 4, energy 4, homogeneity 4, entropy 4, contrast 5, correlation 5, energy 5, homogeneity 5, entropy 5, contrast 6, correlation 6, energy 6, homogeneity 6, entropy 6, contrast 7, correlation 7, energy 7, homogeneity 7, entropy 7, contrast 8, correlation 8, energy 8, homogeneity 8, entropy 8, contrast 9, correlation 9, energy 9, homogeneity 9, entropy 9, contrast 10, correlation 10, energy 10, homogeneity 10, entropy 10, contrast 11, correlation 11, energy 11, homogeneity 11, entropy 11, contrast 12, correlation 12, energy 12, homogeneity 12, entropy 12, coarseness 1, contrast 1, directionality 1, coarseness 2, contrast 2, directionality 2, coarseness 3, contrast 3, directionality 3}.

The latter is based on the difference between the grey level value of pixel qc and the radius R of its circular neighbourhood centred at qc. As a result, the LBP codes are calculated as Eq (16).

$$LBP_{P,R}(q_c) = \sum_{p=0}^{P-1} s(x)2^p \tag{16}$$

Within the circular neighbourhood of radius R and P nearby pixels, x = q_p q_c is the difference between the intensity levels of the neighbouring pixels (q_p) and the centre pixel (q_c). In addition, s(x) is given by Eq (17).

$$s(x) = \{1\ x \geq 0\ 0\ \ otherwise \tag{17}$$

The value of the three attributes, "coarseness-contrast-directionality" (CND) for each pixel, is used to create a Tamura image. This image was created for a combined RGB distribution.

3.4. BPN classifier

Finally, the fused extracted characteristics of MRI and CT are classified as normal, malignant, or benign tumours using the back-propagation method. Because it may vary its weight, it is an adaptable network. There are three levels in a NN: input layers, hidden layers, and output layers. In order to find an ideal number of hidden nodes in a simulation, the number of nodes in hidden layers is adjusted.

The back-propagation learning rule is utilized to alter network weights as well as biases to reduce the network's MSE or cost function. The binary sigmoidal function, or tan-sigmoid, is used to activate each node in the network. This is a widely used function in BPN. This function restricts the output of all network nodes to a range of 0 to 1. MSE for each training iteration for neural networks is taught until it stops decreasing.

Computing the gradient about the parameters can assist us in doing so, as the gradient is defined as a vector of partial derivatives of (w1, w2,..., wh, b1,..., bi). As previously stated, derivatives measure the change in the output of a function about its input. The cost function's gradient indicates which direction (w1, w2,..., wh, b1,..., bi) drops the fastest. Gradient Descent is a common term for this. The machine converges towards the local minimum with each epoch. Automatic differentiation combines the chain rule with massive processing capacity to calculate the gradient from a potentially enormous, complex model. Backpropagation is the name given to this algorithm in reverse. Backpropagation is performed recursively across each layer of the NN. Let us start with the most basic example of a neural network: a network with only one node per layer to see how Backpropagation works. In order to understand Backpropagation, we will consider a neural network with only 2 layers and a single node in each.

The cost function for a single training example is given by Eq (18):

$$J = \frac{1}{2}(a_1^2 - y)^2 \tag{18}$$

We must find the $\partial J/\partial w_{11}^1$ and $\partial J/\partial b^1$ to implement gradient descent in Eqs (19) and (20). To find that, we will use the chain rule.

$$\frac{\partial J}{\partial w_{11}^1} = \left(\frac{\partial J}{\partial a_1^2}\right)\left(\frac{\partial a_1^2}{\partial z}\right)\left(\frac{\partial z}{\partial w_{11}^1}\right) = \left(\frac{\partial\left(\frac{1}{2}(a_1^2-y)^2\right)}{\partial a_1^2}\right)\left(\frac{\partial(g(z))}{\partial z}\right)\left(\frac{\partial(a_1^1 w_{11}^1 + b^1)}{\partial w_{11}^1}\right) = \left((a_1^2 - y)\right)\Big(g(z)\big(1 - g(z)\big)\Big)(a_1^1) = (g(z) - y)\cdot g(z)(1 - g(z))\cdot a_1^1 \tag{19}$$

The derivative of the sigmoid function $g(z)$ can be demonstrated using calculus $(z).\big(1 - g(z)\big)$. J's partial derivative in terms of bias b^1:

$$\frac{\partial J}{\partial b^1} = \left(\frac{\partial J}{\partial a_1^2}\right)\left(\frac{\partial a_1^2}{\partial z}\right)\left(\frac{\partial z}{\partial b^1}\right) = \left(\frac{\partial\left(\frac{1}{2}(a_1^2-y)^2\right)}{\partial a_1^2}\right)\left(\frac{\partial(g(z))}{\partial z}\right)\left(\frac{\partial(a_1^1 w_{11}^1 + b^1)}{\partial b^1}\right) = \left((a_1^2 - y)\right)\Big(g(z)\big(1 - g(z)\big)\Big) = (g(z) - y)\cdot g(z)(1 - g(z)) \tag{20}$$

Here $g(z)$ is simply sigmoid( ). The RHS of Eqs (19) and (20) are known using forward propagation. Thus, the above equations give us the gradients to tweak the parameters while applying gradient descent. This was a simple case of 2 layers with a node in each. We get a network if we increase it to 3 layers with a node in each. Now, in this network, Eqs (19) and (20) can be re-written as:

$$\frac{\partial J}{\partial w_{11}^2} = \left(\frac{\partial J}{\partial a_1^3}\right)\left(\frac{\partial a_1^3}{\partial z^2}\right)\left(\frac{\partial z^2}{\partial w_{11}^2}\right) = \left(\frac{\partial\left(\frac{1}{2}(a_1^3-y)^2\right)}{\partial a_1^3}\right)\left(\frac{\partial\left(g(z^2)\right)}{\partial z^2}\right)\left(\frac{\partial(a_1^2 w_{11}^2 + b^2)}{\partial w_{11}^2}\right) \tag{21}$$

$$= \left((a_1^3 - y)\right)\Big(g(z^2)\big(1 - g(z^2)\big)\Big)(a_1^2) = (g(z^2) - y)\cdot g(z^2)\big(1 - g(z^2)\big)\cdot a_1^2\,\frac{\partial J}{\partial b^2} =$$

$$\left(\frac{\partial J}{\partial a_1^3}\right)\left(\frac{\partial a_1^3}{\partial z^2}\right)\left(\frac{\partial z^2}{\partial b^2}\right) = \left(\frac{\partial\left(\frac{1}{2}(a_1^3-y)^2\right)}{\partial a_1^3}\right)\left(\frac{\partial\left(g(z^2)\right)}{\partial z^2}\right)\left(\frac{\partial(a_1^2 w_{11}^2 + b^2)}{\partial b^2}\right) = \left((a_1^3 - y)\right)\Big(g(z^2)\big(1 - g(z^2)\big)\Big) = (g(z^2) - y)\cdot g(z^2)\big(1 - g(z^2)\big) \tag{22}$$

$$\frac{\partial J}{w_{11}^1} = \left(\frac{\partial J}{\partial a_1^3}\right)\left(\frac{\partial a_1^3}{\partial z^2}\right)\left(\frac{\partial z^2}{\partial a_1^2}\right)\left(\frac{\partial a_1^2}{\partial z^1}\right)\left(\frac{\partial z^1}{\partial w_{11}^1}\right) =$$

$$\left(\frac{\partial\left(\frac{1}{2}(a_1^3-y)^2\right)}{\partial a_1^3}\right)\left(\frac{\partial\left(g(z^2)\right)}{\partial z^2}\right)\left(\frac{\partial(a_1^2 w_{11}^2 + b^2)}{\partial a_1^2}\right)\left(\frac{\partial g(z^1)}{\partial z^1}\right)\left(\frac{\partial(a_1^1 w_{11}^1 + b^1)}{\partial w_{11}^1}\right) \tag{23}$$

$$= \left((a_1^3 - y)\right)\left(g(z^2)\left(1 - g(z^2)\right)\right)(w_{11}^2)\left(g(z^1)\left(1 - g(z^1)\right)\right)(a_1^1)\frac{\partial J}{\partial b^1} =$$

$$\left(\frac{\partial J}{\partial a_1^3}\right)\left(\frac{\partial a_1^3}{\partial z^2}\right)\left(\frac{\partial z^2}{\partial a_1^2}\right)\left(\frac{\partial a_1^2}{\partial z^1}\right)\left(\frac{\partial z^1}{\partial b^1}\right) = \left(\frac{\partial\left(\frac{1}{2}(a_1^3 - y)^2\right)}{\partial a_1^3}\right)\left(\frac{\partial\left(g(z^2)\right)}{\partial z^2}\right)\left(\frac{\partial(a_1^2 w_{11}^2 + b^2)}{\partial a_1^2}\right)\left(\frac{\partial g(z^1)}{\partial z^1}\right)\left(\frac{\partial(a_1^1 w_{11}^1 + b^1)}{\partial b^1}\right) =$$

$$\left((a_1^3 - y)\right)\left(g(z^2)\left(1 - g(z^2)\right)\right)(w_{11}^2)\left(g(z^1)\left(1 - g(z^1)\right)\right)(1) \tag{24}$$

Again the RHS of Eqs (21)–(24) is known. So we can calculate the required gradients. This describes how Backpropagation works mathematically. Now that we've grasped the aforementioned mathematical concepts, we can use this method to backpropagate a simple linear NN. The method stays the same for more complicated NN, with numerous nodes in each layer, and the only variation is that the subscripts and superscripts of *w*, *z*, *a*, and *b* are changed. Backpropagation becomes complicated, and we must use matrix forms of derivatives, i.e., gradient vectors. The core concept, though, stays the same. Backpropagation is just calculating the change in the cost function J as the network's parameters change utilizing the chain rule of derivatives. For data classification tasks, this computes the gradient, which is utilized to change parameters utilizing gradient back propagation neural networks. It supervises the learning process. The problem of error convergence is a significant challenge in supervised learning. The difference between desired and computed values should be as small as possible. The goal is to determine a set of weights that reduces mistakes. BPN classifier had good accuracy, a short learning period, and was resistant to weight changes.

The input brain MRI pictures were classified using a back propagation NN. Features retrieved utilizing PCA, such as mean, median, Variance, correlation, Eigen values and Eigen vectors, are input variables for training the neural network. The backpropagation approach was used to train these networks, an effective tool for data classification applications. For training purposes, a set of database photos is employed.

4. Results and discussion

This study makes use of Python version 2021 software. Preprocessing, image fusion, feature extraction, and picture classification are all steps in the proposed work. BPN classifier Python script has been written for preprocessing, SWT-based image fusion approach, and GLCM feature extraction, and the result has been achieved. The Python inbuilt classification learner application is utilized for testing and analysis with different classifiers. The extracted feature data is saved in an excel file, which is then directly fed into the classification learner programme to examine the effect of picture fusion between proposed and existing classifiers.

4.1. Dataset description

MRI dataset: The MSD challenge's brain tumour dataset is a subset of data utilized in the 2016 and 2017 BraTS competitions [8–10]. 750 multiparametric MRI scans from patients with glioblastoma or lower-grade glioma were included in the study. Native (T1) and post-Gadolinium (Gd) contrast T1-Gd, native T2, and T2-FLAIR volumes were included in each patient's multi-parametric MRI sequences. These MRI scans are collected during ordinary clinical practice at 19 institutions, using

diverse equipment and acquisition techniques, and then aggregated to establish a publicly available benchmark dataset for segmenting brain tumour sub-regions. The scanners used to acquire these scans ranged from 1T to 3 T. Expert board-certified neuroradiologists validated gold standard annotations for all tumour subregions in all scans. The following institutions contributed data to the BraTS dataset: 1) CBICA, University of Pennsylvania, PA, USA; 2) University of Debrecen, Hungary; 6) Henry Ford Hospital, MI, USA; 3) University of Alabama at Birmingham, AL, USA, 4) University Hospital of Bern, Switzerland, 5) Heidelberg University, Germany, 7) University of California, CA, USA, 8) Emory University, GA, USA, 9) MD Anderson Cancer Center, TX, USA, 10) Mayo Clinic, MN, USA, 11) University of North Carolina, NC, USA, 12) Case Western Reserve University, OH, USA, 14) Duke University School of Medicine, NC, USA, 16) Fondazione IRCCS Istituto Neurologico Carlo Besta, Italy, 17) Thomas Jefferson University, PA, USA. Data from institutions 6–16 describe data from TCIA (http://www.cancerimagingarchive.net/)

CT dataset: Multiple slice head CT scan of different subjects is taken for segmentation of BM. Both diseased and normal scans are included in the database. A total of 28 patient datasets with more than 700 slices are considered for this work. The number of slices varies from 23 to 34 for different subjects. The program is designed for complete automation; users must select only the folder containing CT slices. Extracted BM are named after their original name and saved automatically in a new folder in the same path as the source folder. The term "dataset" is used in this research to describe all of a patien's scanned CT slices in one sitting. The number of slices can vary depending on the machine, the practitioner's discretion, and the machine's competence. Moreover, "database" refers to the full data set used in this project.

The accuracy, precision, recall, specificity, F1 score, confusion matrix, and ROC curve are used to evaluate classifier performance. True positive (TP), false positive (FP), true negative (TN), and false negative (FN) are the four possible outcomes in a confusion matrix (FN). This section describes how classifier performance is measured.

Accuracy. The ratio of the number of right guesses to the number of predictions determines the classifier's accuracy. Eq (25), as illustrated below, defines accuracy.

$$Accuracy = \frac{TP+TN}{TP+TN+FN+FP} \tag{25}$$

Precision. The correct prediction ratio to the actual prediction of brain tumour instances depicted is the classifier's precision by Eq (26).

$$Precision = \frac{TP}{TP+FP} \tag{26}$$

Recall. The ratio of accurately predicted brain tumour cases to total brain tumour cases, including non-brain tumour instances, is known as the classifier's recall by Eq (27).

$$Recall = \frac{TP}{TP+FN} \tag{27}$$

Specificity. The ratio of correctly detected nonbrain tumour cases to negative brain tumour instances, which is expressed as in, represents the classifier's specificity by Eq (28).

$$Specificity = \frac{TN}{TN+FP} \tag{28}$$

F1 Score. It is average of classifiers' precision and recall, as described in Eq (29)

$$F1\_Score = \frac{Precisionxrecall}{Precision+Recall} \tag{29}$$

Confusion Matrix. The confusion matrix of the prediction method determines the classifier's performance in matrix form. As illustrated in Figure 4, it contains correctly identified brain tumour cases, misclassified brain tumour findings, correctly identified nontumor cases, and misclassified nonbrain tumour instances.

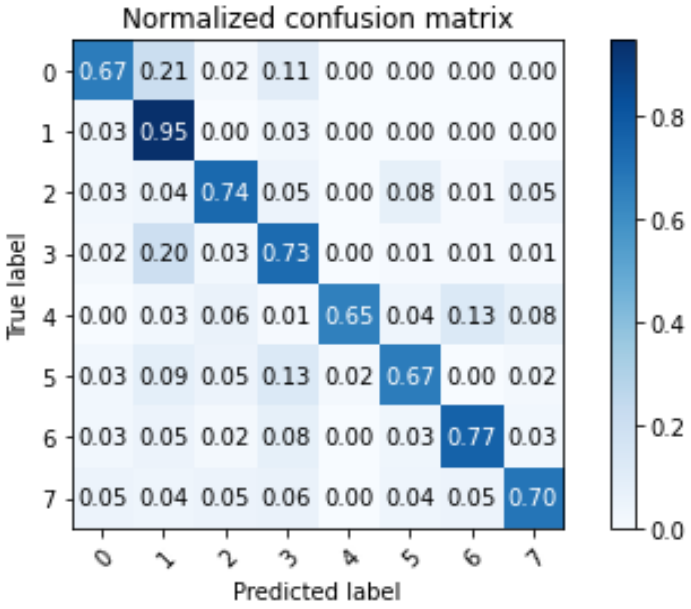

Figure 4. Confusion matrix of proposed tumour detection.

Table 1. Brain image analysis.

Datasets	Input Brain image	Preprocessed Brain image	Decomposed Brain Image	Fused Brain image	Extracted Brain image	Classified Brain image
MRI Dataset	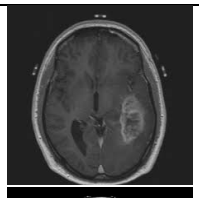	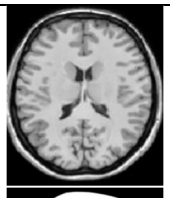		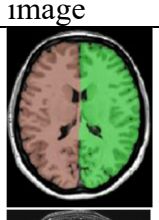		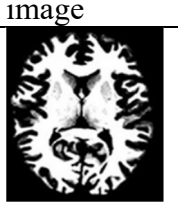
CT Dataset	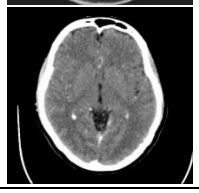		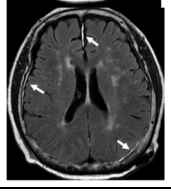	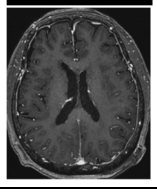	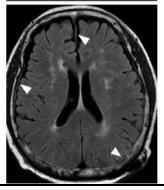	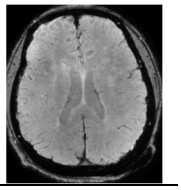

Table 2. Comparative analysis of proposed and existing methods.

Datasets	Techniques	Accuracy	Precision	Recall	Specificity	F-Measure
MRI	MSVD	82	79	65	74	52
Dataset	PCNN	85	83	69	82	55
	GLCM_Tamura_BPN	96	92	83	85	75
CT	MSVD	84	81	68	78	61
Dataset	PCNN	90	85	75	86	65
	GLCM_Tamura_BPN	98	94	89	89	81

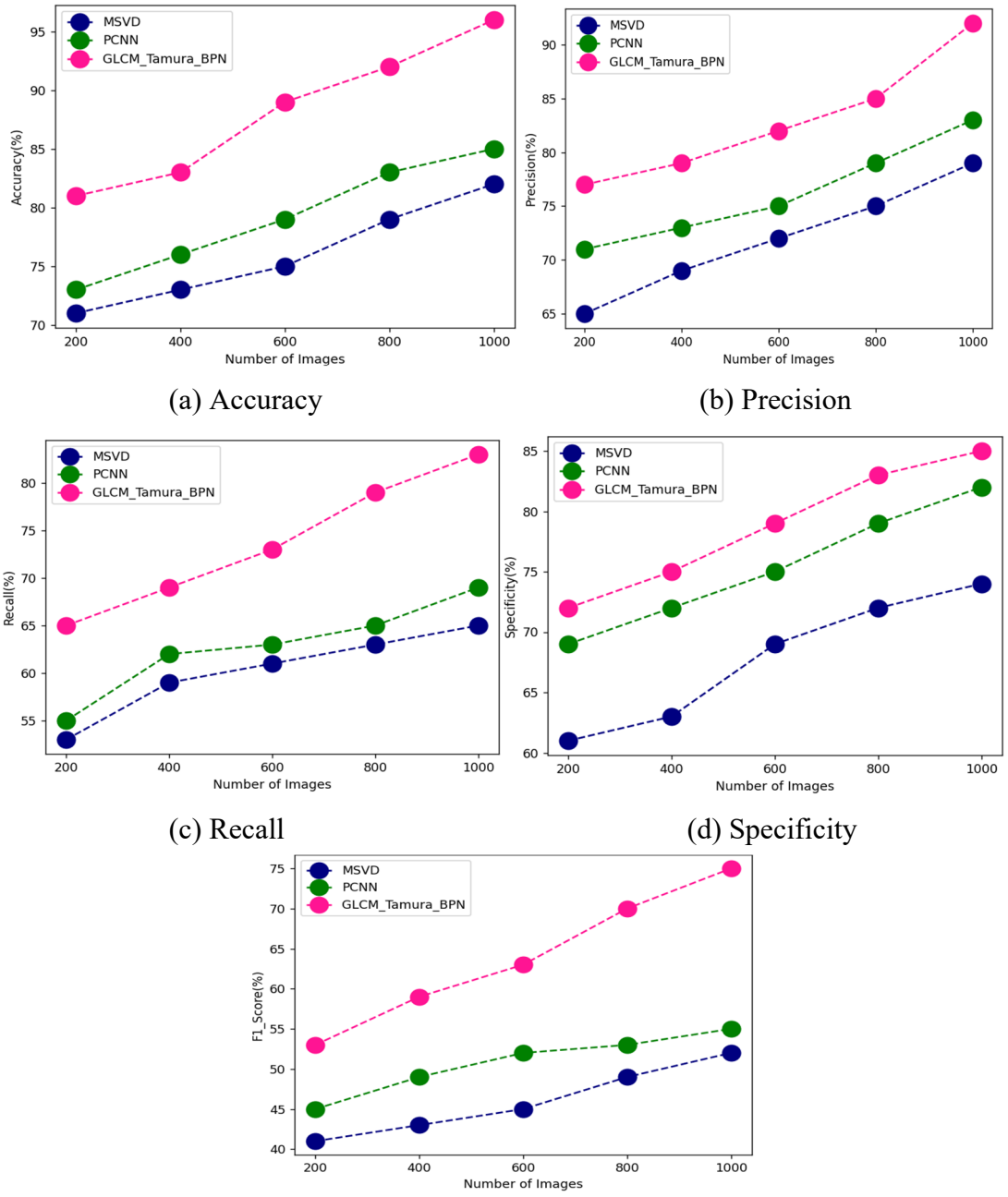

(a) Accuracy (b) Precision

(c) Recall (d) Specificity

(e) F1_Score

Figure 5. Comparison of proposed and existing methods of MRI Dataset of (a) Accuracy, (b) Precision, (c) Recall, (d) Specificity, (e) F1_Score.

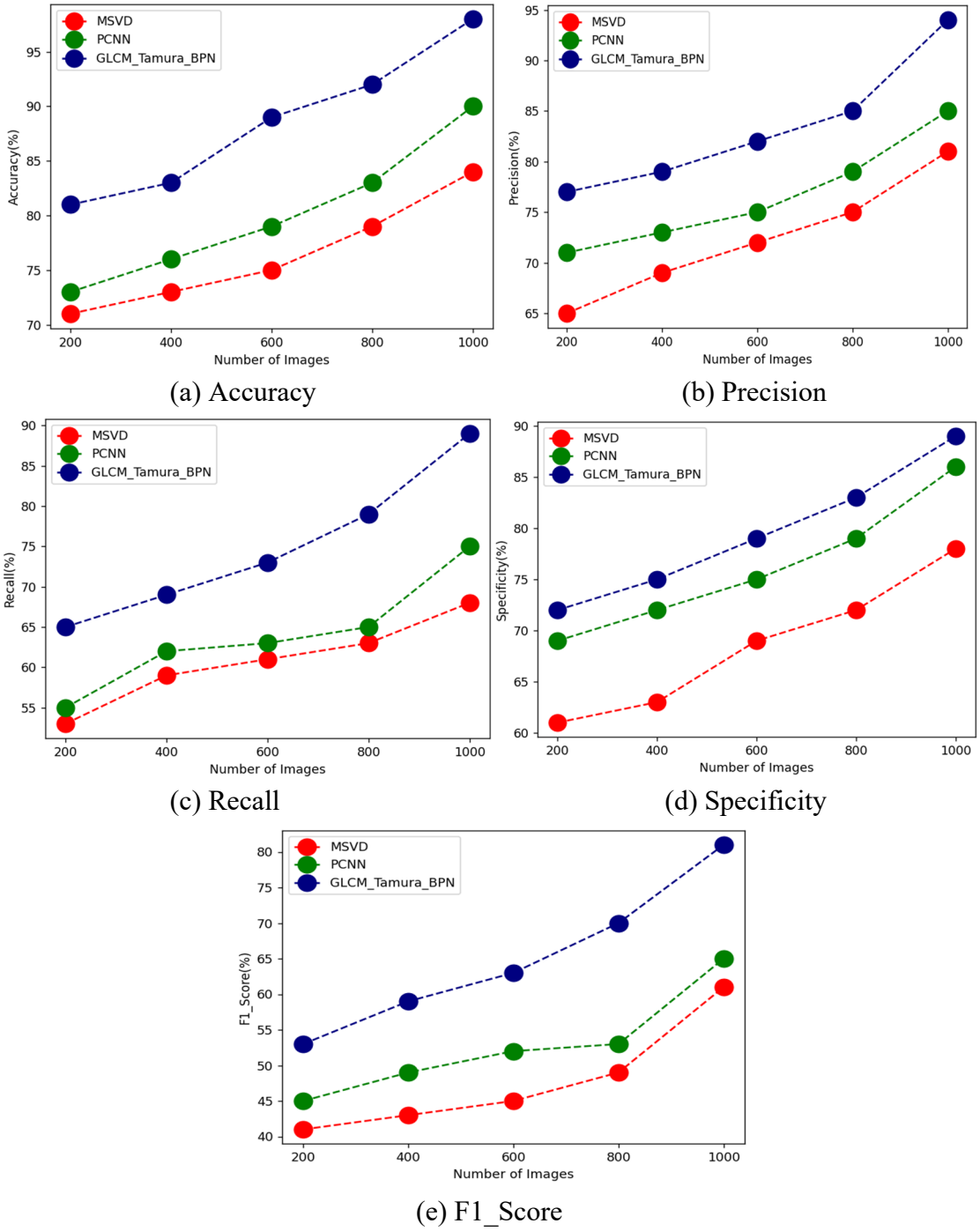

Figure 6. Comparison of various parameters of existing and proposed methods of CT dataset of (a) accuracy, (b) precision, (c) Recall, (d) Specificity, (e) F1_Score.

Tables 1–2 show that the GLCM Tamura BPN classifier outperforms the MSVD and PCNN classifier in accuracy, precision, recall, specificity, and F1 score parameters. The average time is obtained from ten independent trials performed on a PC with an Intel Core 3 processor and a Celeron 3.06G/1G processor. According to tabulated results, the proposed SVM classifier takes longer to execute the results when features from fused images are given as input, almost 420 s, whereas the proposed GLCM Tamura BPN, MSVD, and PCNN classifiers take 128, 160 and 180 s, respectively, when features from MRI/CT fused image alone are given as input. The proposed method takes longer

to execute the results compared to existing methodologies due to the added step. When fused pictures are evaluated for feature extractions and classification, the suggested GLCM Tamura BPN classifier delivers an accuracy of 96%, precision of 92%, recall of 83%, specificity of 85%, and F1 score of 75%, as shown in Figure 5–6. When MRI/CT fused image alone is examined for feature extraction and classification, these 5 parameters have high values and perform better than MSVD and PCNN using proposed GLCM Tamura BPN classifiers.

4.2. Discussion

In magnetic resonance imaging (MRI), a few pictures can be gotten utilizing different imaging settings (for example T1, T2, DWI, and energy). However, these pictures have comparative physical designs with various differences, giving an abundance of data to find. In any case, the pictures under unambiguous imaging settings may not be accessible because of the constraint of examining time or debasement brought about by commotions. It is appealing to determine missing pictures for certain settings from the accessible MR pictures. In the proposed model, the multiscale data is additionally taken on in the antagonistic learning (not simply in the generator or discriminator), so we can create excellent combined pictures. Enlarged convolutions with various widening proportions were utilized to expand the open fields. Furthermore, we integrated the distance guide and shaped data into the division technique to section contacting cores, which is troublesome using conventional division strategies.

5. Conclusions

This research proposes a novel technique to attain increased efficiency. MRI and CT images are chosen and fused after undergoing preprocessing and SWT-based decomposition stage. The fused image is obtained through ISWT. Further features are extracted through the GLCM-Tamura method, fed to the BPN classifier. For picture classification, supervised learning with a non-knowledge-based classifier will be employed. The classifier utilizes trained databases to segregate the tumour as benign or malignant, from which the tumour region is segmented via k-means clustering. After the software implementation, the health status of the patients is notified through GSM. Our method integrates image fusion, feature extraction, and classification to distinguish and further segment the tumor-affected area and to acknowledge the affected person. The experimental analysis has been carried out in terms of accuracy of 96%, the precision of 92%, recall of 83%, specificity of 85%, and F1 score of 75%.

Conflicts of interest

The authors declare that there is no conflict of interest regarding the publication of this paper.

References

1. D. Sara, A. K. Mandava, A. Kumar, S. Duela, A. Jude, Hyperspectral and multispectral image fusion techniques for high-resolution applications: A review, *Earth Sci. Inf.*, **14** (2021), 1685–1705. https://doi.org/10.1007/s12145-021-00621-6

2. X. Feng, L. He, Q. Cheng, X. Long, Y. Yuan, Hyperspectral and multispectral remote sensing image fusion based on endmember spatial information, *Remote Sens.*, **12** (2020), 1009. https://doi.org/10.3390/rs12061009
3. U. Subramaniam, M. M. Subashini, D. Almakhles, A. Karthick, S. Manoharan, An expert system for COVID-19 infection tracking in lungs using image processing and deep learning techniques, *BioMed Res. Int.*, **2021** (2021), 1–17. https://doi.org/10.1155/2021/1896762
4. S. S. Ganesh, G. Kannayeram, A. Karthick, M. Muhibbullah, A novel context-aware joint segmentation and classification framework for glaucoma detection, *Comput. Math. Methods Med.*, **2021** (2021), 1–19. https://doi.org/10.1155/2021/2921737
5. T. Saba, A. S. Mohamed, M. El-Affendi, J. Amin, M. Sharif, Brain tumour detection using fusion of handcrafted and deep learning features, *Cognit. Syst. Res.*, **59** (2020), 221–230. https://doi.org/10.1016/j.cogsys.2019.09.007
6. X. Liu, A. Yu, X. Wei, Z. Pan, J. Tang, Multimodal MR image synthesis using gradient prior and adversarial learning, *IEEE J. Sel. Top. Signal Process.*, **14** (2020), 1176–1188. https://doi.org/10.1109/JSTSP.2020.3013418
7. M. Sharif, J. Amin, M. Raza, M. Yasmin, S. C. Satapathy, An integrated design of particle swarm optimization (PSO) with the fusion of features for detection of brain tumor, *Pattern Recognit. Lett.*, **129** (2020), 150–157. https://doi.org/10.1016/j.patrec.2019.11.017
8. X. Liu, Z. Guo, J. Cao, J. Tang, MDC-net: A new convolutional neural network for nucleus segmentation in histopathology images with distance maps and contour information, *Comput. Biol. Med.*, **135** (2021), 104543. https://doi.org/10.1016/j.compbiomed.2021.104543
9. Z. Hu, J. Tang, Z. Wang, K. Zhang, L. Zhang, Q. Sun, Deep learning for image-based cancer detection and Diagnosis—A survey, *Pattern Recognit.*, **83** (2018), 134–149. https://doi.org/10.1016/j.patcog.2018.05.014
10. H. Kaur, D. Koundal, V. Kadyan, N. Kaur, K. Polat, Automated Multimodal image fusion for brain tumor detection, *J. Artif. Intell. Syst.*, **3** (2021), 68–82. https://doi.org/10.33969/AIS.2021.31005
11. J. Amin, M. Sharif, N. Gul, M. Yasmin, S. A. Shad, Brain tumor classification based on DWT fusion of MRI sequences using convolutional neural network, *Pattern Recognit. Lett.*, **129** (2020), 115–122. https://doi.org/10.1016/j.patrec.2019.11.016
12. R. Nanmaran, S. Srimathi, G. Yamuna, S. Thanigaivel, A. S. Vickram, A. K. Priya, et al., Investigating the role of image fusion in brain tumor classification models based on machine learning algorithm for personalized medicine, *Comput. Math. Methods Med.*, **2022** (2022), 1–13. https://doi.org/10.1155/2022/7137524
13. A. Selvapandian, K. Manivannan, Fusion based Glioma brain tumor detection and segmentation using ANFIS classification, *Comput. Methods Programs Biomed.*, **166** (2018), 33–38. https://doi.org/10.1016/j.cmpb.2018.09.006
14. S. Preethi, P. Aishwarya, An efficient wavelet-based image fusion for brain tumor detection and segmentation over PET and MRI image, *Multimed Tools Appl.*, **80** (2021), 14789–14806. https://doi.org/10.1007/s11042-021-10538-3
15. P. M. Kumar, R. Saravanakumar, A. Karthick, V. Mohanavel, Artificial neural network-based output power prediction of grid-connected semitransparent photovoltaic system, *Environ. Sci. Pollut. Res.*, **29** (2022), 10173–10182. https://doi.org/10.1007/s11356-021-16398-6

16. N. Jeevanand, P. A. Verma, S. Saran, Fusion of hyperspectral and multispectral imagery with regression Kriging and the Lulu operators: A comparison, *Int. Arch. Photogramm. Remote Sens. Spatial Inf. Sci.*, **5** (2018), 583–588. https://doi.org/10.5194/isprs-archives-XLII-5-583-2018
17. V. Chandran, M. G. Sumithra, A. Karthick, T. George, M. Deivakani, B. Elakkiya, et al., Diagnosis of cervical cancer based on ensemble deep learning network using colposcopy images, *BioMed Res. Int.*, **2021** (2021), 1–15. https://doi.org/10.1155/2021/5584004
18. D. Jiang, D. Zhuang, Y. Huang, J. Fu, Survey of multispectral image fusion techniques in remote sensing applications, in *Image Fusion and its Applications* (ed. Y. Zheng), IntechOpen, (2011), 1–23.
19. R. Kabilan, V. Chandran, J. Yogapriya, A. Karthick, P. P. Gandhi, V. Mohanavel, et al., Short-term power prediction of building integrated photovoltaic (BIPV) system based on machine learning algorithms, *Int. J. Photoenergy*, **2021** (2021), 1–11. https://doi.org/10.1155/2021/5582418
20. B. K. Umri, M. W. Akhyari, K. Kusrini, Detection of covid-19 in chest X-ray image using CLAHE and convolutional neural network, in *2020 2nd International Conference on Cybernetics and Intelligent System (ICORIS)*, IEEE, Manado, Indonesia, (2020), 1–5. https://doi.org/10.1109/ICORIS50180.2020.9320806
21. V. Chandran, C. K. Patil, A. M. Manoharan, A. Ghosh, M. G. Sumithra, A. Karthick, et al., Wind power forecasting based on time series model using deep machine learning algorithms, *Mater. Today Proc.*, **47** (2021), 115–126. https://doi.org/10.1016/j.matpr.2021.03.728
22. V. Chandran, C. K. Patil, A. Karthick, D. Ganeshaperumal, R. Rahim, A. Ghosh, State of charge estimation of lithium-ion battery for electric vehicles using machine learning algorithms, *WEVJ*, **12** (2021), 38. https://doi.org/10.3390/wevj12010038

AIMS Press